Comparative stereodynamics in molecule-atom and molecule-molecule rotational energy transfer: NO($A^2\Sigma^+$) + He and D_2.

Thomas F. M. Luxford,[1] Thomas R. Sharples,[1] Dave Townsend,[1,2] Kenneth G. McKendrick[1] and Matthew. L. Costen[1,a]

[1]*Institute of Chemical Sciences, Heriot-Watt University, Edinburgh, EH14 4AS, U. K.*

[2]*Institute of Photonics & Quantum Sciences, Heriot-Watt University, Edinburgh, EH14 4AS, U. K.*

ABSTRACT

We present a crossed molecular beam scattering study, using velocity-map ion-imaging detection, of state-to-state rotational energy transfer for NO($A^2\Sigma^+$) in collisions with the kinematically identical colliders He and D_2. We report differential cross sections and angle-resolved rotational angular momentum polarization moments for transfer of NO(A, v = 0, N = 0, j = 0.5) to NO(A, v = 0, N' = 3, 5-12) in collisions with He and D_2 at respective average collision energies of 670 cm^{-1} and 663 cm^{-1}. Quantum scattering calculations on a literature *ab initio* potential energy surface for NO(A)-He (Kłos *et al*., J Chem Phys **129**, 244303 (2008)) yield near-quantitative agreement with the experimental differential scattering cross sections, and good agreement with the rotational polarization moments. This confirms that the Kłos *et al*. potential is accurate within the experimental collisional energy range. Comparison of the experimental results for NO(A) + D_2 and He collisions provides information on the hitherto unknown NO(A)-D_2 potential energy surface. The similarities in the measured scattering dynamics of NO(A) imply that the general form of the NO(A)-D_2 potential must be similar to that calculated for NO(A)-He. A consistent trend for the rotational rainbow maximum in the differential cross sections for NO(A) + D_2 to peak at more forward angles than those for NO(A) + He is consistent with the NO(A)-D_2 potential being more anisotropic with respect to NO(A) orientation. No evidence is found in the experimental measurements for coincident rotational excitation of the D_2, consistent with the potential having low anisotropy with respect to D_2. The NO(A) + He polarization moments deviate systematically from the predictions of a hard-shell, kinematic-apse scattering model, with larger deviations as N' increases, which we attribute to the shallow gradient of the anisotropic repulsive NO(A)-He potential energy surface.

I. INTRODUCTION

Rotational energy transfer is a ubiquitous molecular process in the gas phase, which has been the subject of extensive study by both experiment and theory.[1, 2] Molecules that have seen detailed experimental and theoretical study include open-shell species important in combustion and atmospheric chemistry, particularly the NO and OH radicals, in both ground and excited electronic states.[3, 4] As a result they can be regarded as benchmark species for comparisons of theoretical predictions

[a] Author to whom correspondence should be addressed. Electronic mail: m.l.costen@hw.ac.uk

from scattering calculations to experimental measurements, providing tests of scattering theory, and of potential energy surfaces (PESs) derived from electronic structure theory.

Stereodynamics measurements have proved particularly useful for detailed testing of theory, rather than more averaged scalar measurements such as rotational energy transfer (RET) rate constants.[5] In particular, measurements of state-resolved differential scattering cross sections (DCSs) and scattering angle-resolved rotational angular momentum polarization provide stringent tests of the state-of-the-art theory. In recent years, the benchmark experimental approach has combined crossed molecular beam (CMB) preparation of the collision partners, with product detection by resonance-enhanced multi-photon ionization (REMPI) and velocity-map imaging (VMI) of the resulting ions.[6] There is a close correlation between the resulting image and the scattering Newton diagram for the collision, allowing facile determination of the DCS, and with appropriate control of the probe laser polarization and choice of REMPI spectroscopic transition the angular momentum polarization may be determined as a function of the scattering angle.[7-9] This CMB-VMI approach, which superseded earlier work using spatial imaging,[10, 11] has been applied systematically to the collisions of NO($X^2\Pi$) + He, Ne, Ar, and Kr, as well as CO($X^1\Sigma^+$) + He and Ne, and OH($X^2\Pi$) + He and Ar.[7-9, 12-28] However, measurements at this level of detail for collisions with *molecular* partners are very rare. This is probably an indication of the difficulties introduced by the additional complexity of molecule-molecule collisions, both in molecular beam preparation of the colliders and analysis of the results of experiments, and in theory, where both scattering and PES calculations are much more challenging. This is a notable deficiency, though, as most of the systems of practical interest in combustion or atmospheric chemistry naturally involve molecule-molecule collisions, and there is thus a strong desire to improve our understanding and modeling of these systems.

Whilst there are some pioneering reports of DCSs for molecule-molecule RET using CMB with rotatable detectors using either universal mass-spectrometric or REMPI detection, it is only recently using the CMB-VMI approach that more systematic studies have appeared.[29-32] This has included HCl colliding with N_2 and CH_4, where clear evidence of rotation-rotation (R-R) correlations were observed, as well as the first measurements of DCSs for polyatomic + diatomic collisions, namely ND_3 + H_2 and CH_3 + H_2, D_2 and N_2.[33-37] Most directly relevant to this report, the CMB-VMI technique has been applied to NO(X) + D_2, both with, and without, hexapole selection of the pre-collision rotational state.[38, 39]

All of the measurements in these previous literature reports involved molecules in their *ground* electronic states. We have recently shown that it is possible to extend the CMB-VMI technique to study the collisions of electronically excited molecules in short-lived *excited* states, specifically NO in its first excited state, $A^2\Sigma^+$.[40-43] NO(A) is formed directly in some high energy environments,[44, 45] and whenever NO(X) is probed using laser-induced fluorescence, including in important environments such as combustion systems, the atmosphere, and technological plasmas, where it will undergo collisions with

the surrounding atoms and molecules during its ~ 200 ns fluorescence lifetime.[46, 47] In our experimental approach, NO is excited in the molecular beam crossing region *via* the $Q_1(0.5)$ transition of the A-X(0,0) band. This pulsed excitation not only prepares a single initial rovibronic state, NO(A, v = 0, N = 0, j = 0.5), but also provides a well-defined start time for the inelastic scattering, substantially simplifying the data analysis compared to conventional CMB experiments. After a short interval, typically ~ 400 ns, the NO(A, v = 0, N') products of RET with the collider species are state-selectively probed using VMI in a 1 + 1' REMPI process via the $E^2\Sigma^+$-$A^2\Sigma^+$(0,0) band. In our previous measurements of scattering of NO(A) with He, Ne and Ar, we have demonstrated that this approach can measure state-to-state DCSs for RET, and for Ne and Ar we have also shown that it is sensitive to scattering angle-resolved rotational alignment moments.[40-43]

The simplest molecular collider, H_2, has been used in a number of previously studied systems, including with NO(X), as previously discussed. As an initial step towards studying molecule-molecule inelastic scattering with resolution of the product DCS and scattering angle-resolved rotational angular momentum alignment, performing experiments using both D_2 and He provides the opportunity to compare the scattering dynamics of systems with the same kinematics, but different degrees of freedom and PESs.[38, 39] We present here a study of rotationally inelastic scattering of NO($A^2\Sigma^+$, v = 0, N = 0, j = 0.5) with He and D_2 at average collision energies of 670 cm^{-1} and 663 cm^{-1}, respectively. We apply our CMB-VMI approach to collisions of electronically excited NO, and report DCSs and scattering angle-resolved rotational alignment moments for the product rotational states N' = 3, 5-12. We also present the results of new close-coupled quantum scattering (QS) calculations for NO(A)+He on a literature *ab initio* PES.[48] We discuss the observed scattering dynamics in the context of the QS calculations and in comparison between the colliders, with reference to the literature measurements of NO(X) + He/D_2 scattering dynamics.[38, 39]

II. METHODS

A. Experiment

The CMB-VMI experimental setup has been described in detail previously, and therefore only essential details are provided here.[43] Two skimmed molecular beams intersected at the center of a differentially pumped scattering chamber. Different molecular beam source conditions were used to achieve very similar collision energies for the two collider species. In experiments with He as the collider, the 10% NO (99.5%, BOC) in Ne (99.999%, BOC) molecular beam, generated with a backing pressure of 3 bar, had a mean speed of 807 ms^{-1} with a FWHM of 57 ms^{-1}. The molecular beam of He (99.999%, BOC) was generated from a heated pulsed valve (343 K) at a backing pressure of 5 bar, giving a mean speed of 1973 ms^{-1} and a FWHM of 101 ms^{-1}. For experiments with D_2, 10% NO was seeded in Ar (99.998%, BOC) at a backing pressure of 3

bar, to give a mean speed of 605 ms^{-1} with FWHM of 52 ms^{-1}, while the molecular beam of D_2 (99.8%, BOC) was generated at a backing pressure of 5 bar from a room temperature (295 K) pulsed valve, to give a mean speed of 2032 ms^{-1}, with a FWHM of 99 ms^{-1}. This resulted in Gaussian distributions for the center of mass collision energies, with a mean of 670 cm^{-1} and FWHM of 64 cm^{-1} for He, and a mean of 663 cm^{-1} and FWHM of 59 cm^{-1} for D_2, respectively. Additional information on the methods used to determine these speeds, and investigation of the rotational distribution of D_2 in the molecular beam, are provided in the Supplementary Material.[49]

In the crossing region of the two molecular beams, NO(A, v = 0, N = 0, j = 0.5) was prepared by excitation on the $Q_1(0.5)$ transition of the A-X(0,0) band at 226.18 nm, using the frequency-doubled output of a Nd:YAG pumped dye laser (Sirah CTSG/Continuum Surelite II-10). The excitation laser beam was unfocussed, with a diameter of 2 mm, and a fluence of 0.65 mJ cm^{-2}. After a 400 ns delay, during which the prepared NO(A) underwent collisions with either He or D_2, the scattered NO(A, v = 0, N') molecules were probed in a (1 + 1′) REMPI scheme. A second Nd:YAG pumped dye laser (Sirah CSTR-DA24/Continuum Surelite I-10) excited NO(A) on the R-branch of the $E^2\Sigma^+$-$A^2\Sigma^+$ (0,0) band around 600 nm, and the E-state was subsequently ionized by a 532 nm photon. The spin-rotation splitting in the E-A(0,0) band is much smaller than the Doppler width of the transitions, and hence the R_1 and R_2 transitions probing the $j' = N' \pm 0.5$ spin-rotation states cannot be resolved. Thus, whilst the pump scheme prepares a single spin-rotation state, j, the probe scheme only resolves the nuclear rotation, N'. This is not a limitation in the experiments, as the electron spin is (to a very good approximation) a spectator to the collision, and hence spin-rotation state resolution of the products would not yield any additional information on the collision dynamics. The probe beam counter-propagated relative to the pump beam, bisecting the angle made by the molecular beams. The probe beam was either horizontally (H) or vertically (V) polarized in the laboratory frame, with active control applied using a photo-elastic modulator (PEM-90, Hinds Inc.). Two ionization beams were used, one that co-propagated with the probe through the PEM, but that had polarization orthogonal to the probe, and one that was horizontally polarized, and propagated perpendicular to the probe and pump beams. This provided ionization with polarization along two directions in space, but consistently orthogonal to the probe polarization, minimizing any signal dependence on the polarization of the ionization beam. Both the probe and ionization laser beams were unfocussed, with diameters of 3 mm. The probe beam had a fluence of 0.65 μJ cm^{-2}, while the fluence of the ionization beams was varied in the range 4-40 mJ cm^{-2}, with the higher fluences used when detecting high-N' product states with small scattering cross sections. The NO^+ ions produced by the REMPI scheme were velocity mapped onto a micro-channel plate (MCP) detector. The voltage applied across the MCPs was pulsed (100 ns width) using a fast high-voltage switch (DEI PVX4140), to discriminate against ions other than those produced by the NO(A) probe scheme, and in particular, against those resulting from 1+1 REMPI of NO(X) by the pump laser.

Scattering images were acquired for both probe polarizations, together with background images in which the collider molecular beam was delayed by 1 ms and therefore effectively absent, in an interleaved cycle. The wavelength of the probe laser was step-scanned over the transition to remove Doppler selection, in 14 steps of length 5×10^{-4} nm. 200 laser shots were acquired in each phase of the measurement cycle at each wavelength point, with the wavelength scan repeated 5 times. Finally, 4 independent measurements were made for each final N' state on different days.

B. Theory

Close-coupled quantum scattering calculations for NO(A) + He were performed using the Hibridon suite of codes to obtain DCSs and scattering angle-dependent rotational angular momentum alignment moments for each final N' probed experimentally.[50] These moments are expressed in the Hertel-Stoll normalization, referenced to the molecular scattering frame, for which the z-axis lies parallel to the initial relative velocity, **k**, and the final relative velocity, **k'**, lies in the xz-plane, and their definitions are given in Table I.[51] The calculations employed the PES of Kłos *et al.*, which was generated using the spin-restricted coupled cluster method with single, double and perturbative triple excitations (RCCSD(T)).[48] Polar contour and Legendre moment projections of this PES are presented in the Supplementary Material.[49] An NO(A) rotational basis up to $N = 19$ was employed, with NO(A) treated as a rigid rotor with rotational constants $B = 1.987$ cm^{-1} and $\gamma = -0.0027$ cm^{-1}.[52] Calculations were performed for partial waves with $J_{tot} \leq 200.5$, using hybrid log-derivative/Airy propagation of the solution to the close-coupled equations from 4.6 to 200 Bohr. DCSs for each N' were calculated as the sum of those for the two spin-rotation split levels $j = N \pm ½$, and the scattering-angle dependent alignment moments for each N' were calculated as the DCS-weighted average of the relevant spin-rotation level moments. Calculations were performed for individual collision energies at 10 cm^{-1} intervals between 583 and 763 cm^{-1} and averaged over the experimental collision energy distributions, as determined through Monte-Carlo simulations employing the experimental collider velocity distributions.

We have also performed calculations using the kinematic apse (KA) model to predict independently the scattering-angle dependent alignment moments.[53] The KA model assumes scattering from a hard-shell potential, which results in conservation of angular momentum in the direction of the KA, given by, $\mathbf{a_k} = \mathbf{k'} - \mathbf{k} / | \mathbf{k'} - \mathbf{k} |$. For a non-rotating initial state this yields product state rotational alignment moments that are determined purely by the scattering angle and the kinematics of the collision, and are independent of the shape of the PES. These calculations were averaged over the experimentally determined collision energy distributions for both the NO(A)+He and NO(A)+D_2 systems, with the assumption that no internal energy change in D_2 occurred during the collision.

C. Data Analysis

We have employed an iterative basis image simulation and back-fitting methodology for the extraction of the DCSs and polarization moments from the experimental images. Our approach builds upon that described in a previous publication,[43] but has been extended to determine the scattering-angle dependent alignment moments from images, in addition to DCSs.

The probability that a given NO(A) molecule is scattered with polar and azimuthal scattering angles $\omega = (\theta,\phi)$ and is detected using our (1+1') ionization scheme is proportional to:

$$I = \frac{d\sigma}{d\omega}(\theta) \times I_{\text{det}}\left(\phi, \mathbf{k}, A_{q+}^{\{2\}}(\theta), \chi\right) \tag{1}$$

$$I_{\text{det}}\left(\phi, \mathbf{k}, A_{q+}^{\{2\}}(\theta), \chi\right) = 1 + h^{\{2\}}\overline{g}^{\{2\}}\left(1 + F_0^{\{2\}}A_0^{\{2\}}(\theta) + F_1^{\{2\}}A_{1+}^{\{2\}}(\theta) + F_2^{\{2\}}A_{2+}^{\{2\}}(\theta)\right) \tag{2}$$

where **k** is the initial relative velocity vector, χ is the angle between the scattering plane and the electric polarization vector of the probe laser, and $A_{q+}^{\{2\}}(\theta)$ are the non-zero second-rank scattering angle-dependent polarization moments. The $F_q^{\{2\}}$ pre-multipliers are geometrical terms given previously by Brouard *et al.*,[9] $h^{\{2\}}$ is the second-rank polarization sensitivity factor for one-photon probing,[54] and $\overline{g}^{\{2\}}$ is the appropriate time-averaged fine/hyperfine depolarization factor for Hund's case $b_{\beta J}$ coupling.[55-57]

Basis images were simulated using a Monte-Carlo procedure extended from one described in a previous publication, and only a brief summary is presented here.[43] NO and He or D_2 speeds were selected from appropriate Gaussian distributions. In our previous work, we assumed that the initial NO and collider trajectories were strictly orthogonal, along the *z* and *x* axes of the laboratory frame, respectively. In this work, the Monte-Carlo procedure was extended to include non-orthogonal trajectories, modelling the finite angular ranges selected by the pump laser beam. Further details are provided in the Supplementary Material.[49] Laboratory-frame product velocities were then calculated using the initial collider velocities, product *N′* rotational state energy, and collider-appropriate kinematics. It was assumed that no change in rotational energy of the D_2 occurred during the collisions. As will be shown in Section III below, this proved to be an excellent assumption. The effect of ionisation-induced recoil was simulated by adding an 8.5 ms^{-1} recoil velocity chosen from an isotropic angular distribution to each final velocity. The resulting simulated ion-strike was then binned into the appropriate detector pixel, (*a*,*b*), based on an independent velocity calibration of the imaging apparatus.[49] The information necessary to construct an image given a DCS and set of polarization moments was then stored for each trajectory; this comprises the pixel coordinate

on the detector, the polar scattering angle and the values of the factors for H and V probe geometries. Typically 10^7 trajectories were stored for use in fitting.

A two stage iterative fitting procedure was employed to extract the DCS and $A_{q+}^{\{2\}}(\theta)$ from the images. This procedure assumed that DCS and alignment moments could be treated as separable in their respective contributions to the images, an assumption that was strongly supported by our previous measurements of NO(A) + Ar scattering.[43] In the first stage, the $A_{q+}^{\{2\}}(\theta)$ moments were assumed to be fixed distributions, e.g. resulting from the QS calculations or KA model, and the DCS was described by a linear combination of m_{DCS} Legendre polynomials in the cosine of the scattering angle, $P_\lambda(\cos\theta)$. The intensity at pixel (a,b) can then be expressed as:

$$I(a,b) = \sum_{\lambda=0}^{m_{DCS}-1} c_\lambda I_\lambda(a,b) \tag{3}$$

where each basis image $I_\lambda(a,b)$ corresponds to the λ^{th}-order Legendre polynomial in the expansion of the DCS, with coefficient c_λ. The basis images were obtained from the set of trajectories generated in the Monte-Carlo simulation, the intensity in each pixel (a,b) being a sum over all n_{ab} trajectories corresponding to that pixel:

$$I_\lambda(a,b) = \sum_{i=1}^{n_{ab}} P_\lambda(\cos\theta_i) I_{\mathrm{det}}\left(\phi_i, \mathbf{k}_i, A_{q+}^{\{2\}}(\theta_i), \chi\right) \tag{4}$$

The images were then convoluted with a 2-D Gaussian function chosen to model the detector response to individual ion strikes, and minor aberrations arising from the ion-optics. The coefficients c_λ were obtained using a downhill simplex χ^2-minimization fit of the simulated images to both the H and V experimental images, with the DCS constrained to remain positive.[58] Although the results of QS calculations for the NO(A) + He system were generally used to provide the initial starting point for the expansion coefficients of the DCS and the assumed $A_{q+}^{\{2\}}(\theta)$, it was verified for a range of N' that an isotropic DCS and isotropic $A_{q+}^{\{2\}}(\theta)$ initial distributions returned the same final results. Restarts of the simplex fit were performed to ensure that the simplex fit explored the full parameter space, with retention of the best-fit simplex vertex and the other λ simplex vertices chosen to reproduce random positive DCSs. This cycle of DCS-fitting was completed when successive simplex minimizations produced χ^2-values that met a pre-set tolerance condition, itself set after an exploration of the convergence properties of the fitting methodology with sample representative data sets.

The DCS resulting from this first stage was then assumed in the second stage, in which basis images were simulated and fit to the experimental images to extract the polarization moments. The image was decomposed as:

$$I(a,b) = I'(a,b) + \sum_{\lambda=0}^{m_{20}-1} c_\lambda^0 I_\lambda^0(a,b) + \sum_{\lambda=0}^{m_{21}-1} c_\lambda^1 I_\lambda^1(a,b) + \sum_{\lambda=0}^{m_{22}-1} c_\lambda^2 I_\lambda^2(a,b) \tag{5}$$

where

$$I'(a,b) = \sum_{i=1}^{n_{ab}} \frac{d\sigma}{d\omega}(\theta_i) \tag{6}$$

Each of the m_{2q} basis images $I_\lambda^q(a,b)$ corresponds to the λ^{th} order Legendre polynomial in an expansion of the moment $A_{q+}^{\{2\}}(\theta)$, with coefficient c_λ^q. The basis images were obtained from the Monte-Carlo simulation as:

$$I_\lambda^q(a,b) = \sum_{i=1}^{n_{ab}} \frac{d\sigma}{d\omega}(\theta_i)\, h^{\{2\}} \bar{g}^{\{2\}} F_q^{\{2\}} P_\lambda(\cos\theta_i) \tag{7}$$

The c_λ^q coefficients were once again obtained through a simplex χ^2-minimzation, including simplex restarts, as described above. The three $A_{q+}^{\{2\}}(\theta)$ moments were constrained to lie within their physical limits, as given in Table I. Finally, the values of the $A_{q+}^{\{2\}}(\theta)$ moments obtained from this second stage were then employed in a repeat fit to the DCS in the first stage, and the entire procedure was iterated until satisfactory agreement between the fitted values for the DCS and all $A_{q+}^{\{2\}}(\theta)$ moments was achieved on successive fitting cycles. Agreement was held to be satisfactory when the maximum absolute difference in the values of the DCS and each polarization moment returned from successive fitting cycles was < 1% of their respective maximum absolute values, differences which are insignificant relative to the experimental error. For each product N', we report the mean of fits to four individual pairs (H and V) of images acquired on different days, and quote errors as twice the standard error of the mean from these individual fits.

III. RESULTS

Figure 1 shows Newton diagrams for the collisions of NO(A) with He and D_2, superimposed on the sum of 4 pairs of H and V experimental images for $N' = 8$. This figure illustrates how through careful manipulation of He and NO beam speeds we were able to prepare systems with essentially identical relative collision vectors, **k**. Note that the probe laser propagation

direction, $\mathbf{k_p}$, bisects the right angle between the molecular beams, making angles of 67° and 61° with **k** for He and D_2, respectively. Because this angle is not close to 0° or 90°, the $F_{1+}^{\{2\}}$ parameter will be non-zero, and we will have a measureable sensitivity to the $A_{1+}^{\{2\}}(\theta)$ moment.[9]

Figure 2 shows an example single set of the experimentally acquired H and V images for collisions of NO(A) with He for the product states N' = 3, 5-12, respectively, alongside the fitted images resulting from the procedure described in II.C. The experimental data show, regardless of probe polarization, a single maximum and a clear and systematic trend with increasing N' for this maximum to move backwards. As required by conservation of energy, the diameter of the scattering ring decreases with increasing N'. The differences in intensity between the V and H images across all final states, particularly large for N' = 8-12, indicates strong rotational angular momentum polarization. The prominent reflection asymmetry about **k** of both the V and H images is a result of our sensitivity to the $A_{1+}^{\{2\}}(\theta)$ moment, and is not the result of a build-up of slow moving molecules, as observed in ground-state inelastic scattering experiments. The fitted images have an excellent level of agreement with the experimental images, indicating that the simulations and fitting procedure successfully reproduce the main features of the scattering dynamics. In the forward direction of some of the experimental images, a localised area of noise can be seen. This is caused by imperfect subtraction of the beam spot, which arises from non-resonant 2-photon ionisation of unscattered NO(A).[43] This effect becomes more prominent for higher-N' product states, as the fluence of the 532 nm ionisation laser was increased to compensate for the much smaller relative population of these states. Pixels affected by this subtraction problem were excluded from the fitting procedure, and the DCS and $A_{q+}^{\{2\}}(\theta)$ moments for the scattering angles affected are not reported. Within the limitations of our experimental signal-to-noise, there does not appear to be any significant scattering amplitude in the affected regions.

Figure 3 shows a corresponding single set of experimental data for the V and H geometries, together with the fitted images, from collisions with D_2 for product states N' = 3, 5-12, respectively. The experimental images in Fig. 3 are remarkably similar to those observed for collisions with He in Fig 2, showing all the same main, qualitative, features. On close inspection, the scattered intensity for all N' in Fig. 3 is consistently more forwards than that observed in Fig 2. We again note that the fitting procedure assumes that no rotational energy change has occurred in the D_2 collider, an assumption which is strongly supported by the excellent agreement between data and fit.

The fitted DCSs and $A_{q+}^{\{2\}}(\theta)$ moments for the NO(A) + He system are compared to the results of QS and KA calculations in Fig. 4. The fitted DCSs have been area normalised to the results of the NO(A)-He quantum scattering

calculations for comparison. Consistent with the measured images, the QS DCS generally displays a single maximum in each N', which shifts to more backward angles as N' increases. There is near-quantitative agreement between the experimental and QS DCSs across all final states. There is also good agreement between the experimental and QS values for $A_0^{\{2\}}(\theta)$, both of which are increasingly to the negative side of the KA prediction as N' increases, with the exception of $N' = 12$ where the low signal-to-noise makes determination of the alignment moments challenging. There is qualitative agreement between experiment and the QS calculations for $A_{2+}^{\{2\}}(\theta)$ within experimental error, which also show systematic deviations from the KA prediction, but there is only broad agreement in the sign of $A_{1+}^{\{2\}}(\theta)$, where experiment is consistently more positive than the QS and KA predictions. Note that in angular regions where the DCS is small the uncertainties in the measured $A_{q+}^{\{2\}}(\theta)$ are necessarily larger. In addition, in the extreme forward and backward directions the experimental sensitivity to $A_{2+}^{\{2\}}(\theta)$ and $A_{1+}^{\{2\}}(\theta)$ decreases, as scattering at all azimuthal angles is compressed into a small range of pixels. In addition, the **k**, **k'** plane to which the polarization moments are referenced is ill-defined for scattering angles of 0° or 180°, and the $A_{1+}^{\{2\}}(\theta)$ and $A_{2+}^{\{2\}}(\theta)$ moments must therefore tend to zero by symmetry, although this is not applied as a constraint in the fitting algorithm used in this work. Consequently, the reported values for the DCS and $A_{q+}^{\{2\}}(\theta)$ moments at 180° are strongly correlated, reflected in the substantial error bars reported for this scattering angle.

Figure 5 compares the DCSs and $A_{q+}^{\{2\}}(\theta)$ moments for the NO(A) + D_2 system to those measured for NO(A) + He, and to predictions from the KA model. The experimental DCSs for NO(A) + D_2 have been area-normalised to the NO(A) + He DCS. As expected from inspection of the experimental images, the DCSs are found to have a single maximum that shifts to more backward scattering as N' increases. Also consistent with the data in Fig. 2 and 3, the fitted DCSs for NO(A) + D_2 are consistently more forward scattered than the corresponding NO(A) + He DCSs, across all product N'. The $A_0^{\{2\}}(\theta)$ moment for NO(A) + D_2 is found to be consistently less negative than that measured for NO(A) + He, and more similar to the predictions from the KA model. The $A_{1+}^{\{2\}}(\theta)$ and $A_{2+}^{\{2\}}(\theta)$ moments are, within their larger reported uncertainties, in broad agreement for He and D_2.

IV. DISCUSSION

We first discuss the results of the NO(A) + He experiments in the context of the theoretically predicted DCSs and $A_{q+}^{\{2\}}(\theta)$ moments. We start with the DCSs. The only previous measurements of NO(A) + He DCSs were of a more limited range of product N' states, and were performed at a mean collision energy 382 cm^{-1}.[41] Within their relatively poor signal-to-noise, they had shown qualitative agreement with the results of QS calculations, confirming that the general form of the PES reported by Kłos *et al* was correct.[48] The substantial range of product N' reported in this study, and the much better signal-to-noise of the current data, combined with a complete polarization-sensitive analysis of the data, enables us to make a much more stringent test of the accuracy of the PES. The excellent, near quantitative, level of agreement between the experimentally determined DCSs and the collision energy-averaged QS calculations for all final product N' states, implies that the features of the PES reported by Kłos *et al*. that determine the DCS are quantitatively correct within the collision energy range sampled.[48]

Turning to the alignment moments, we observe generally very good agreement for the $A_0^{\{2\}}(\theta)$ moment between the experiment and QS theory, with disagreements mostly limited to scattering angles where the DCS is negligible, and the alignment moments are correspondingly difficult to determine accurately. Both experiment and QS theory display increasing disagreement, as a function of increasing N', with the KA model predictions across the range $\theta = 45°$ to 135°, with agreement outside this range presumably arising from the constraint imposed by angular momentum conservation, which results in $A_0^{\{2\}}(\theta) = -1$ for $\theta = 0°$ and 180°.[59] For the $A_{2+}^{\{2\}}(\theta)$ moment the experimental and QS agreement is also good, and although the precision of the measurement of $A_{2+}^{\{2\}}(\theta)$ is lower than that of $A_0^{\{2\}}(\theta)$, we again see systematic deviations from the KA model predictions. The good agreement of the QS calculations with the experiment are further evidence that the PES is a very accurate representation of the NO(A)-He system.

We have previously reported substantial oscillations in the polarization moments as a function of scattering angle for NO(A) + Ne and NO(A) + Ar scattering, observed in both experiments and QS calculations, that cannot be reproduced by the KA model.[40, 43] This is in contrast to equivalent measurements for NO(X) + Rg scattering, where the polarization moments have been found to closely follow hard-shell predictions.[7, 9, 17] The limited non-KA behavior that has been reported for NO(X) + Kr scattering has been attributed to the effect of the attractive regions of the PES.[16] The NO(A)-He PES has a calculated attractive well depth of less than 1 cm^{-1}, which is very unlikely to have a significant impact on the dynamics at the collision energies in this study. However, the repulsive gradient of the NO(A)-He PES is relatively shallow in the collision energy range accessed here, compared to that calculated for NO(X)-He. For example, the potential range 100 – 700 cm^{-1} spans a radius, ΔR, greater than 1 Å for NO(A)-He, compared to an equivalent $\Delta R \approx 0.25$ Å for the NO(X)-He system.[48, 60]

We therefore also attribute the non-KA behavior observed here in experiment and QS calculations for the NO(A)-He system in Fig. 4 to the same fundamental origin as the similar behavior reported for the NO(A)-Ne and NO(A)-Ar systems.[40, 43] Viewed from a classical perspective, collisions that lead to high-N' products come from a smaller range of impact parameters, and must necessarily have probed higher energy regions of the potential than more glancing high-impact parameter collisions that can lead to low-N' products. The trend for increasingly non-KA behavior with increasing N' therefore perhaps reflects the increasing contribution of non-sudden strong interactions over a wide range of R for the collisions that lead to high- N' products.

Returning to the experimental measurements of $A_0^{\{2\}}(\theta)$, for N' = 8-12, where there is appreciable population at θ = 180°, we find that $A_0^{\{2\}}(\theta)$ = -1 within experimental error, in all cases. There is no constraint applied by the fitting algorithm to $A_0^{\{2\}}(\theta)$, other than that it must lie between its high-N physical limits -1 ≤ $A_0^{\{2\}}(\theta)$ ≤ +2. As noted above, a limiting negative $A_0^{\{2\}}(\theta)$ for extreme forwards or backwards scattering is required by conservation of angular momentum. This can be summarized as follows: neglecting the electron spin, which as previously discussed, acts as a spectator to the collision, the prepared NO(A) molecules have initial rotational angular momentum, N = 0, and hence the total angular momentum, $\boldsymbol{J}$, before collision is equal to the orbital angular momentum, $\boldsymbol{L}$, which is necessarily perpendicular to **k**. Scattering exactly backwards requires that the post-collision orbital angular momentum, $\boldsymbol{L'}$, is perpendicular to (the antiparallel) **k'** and **k**, and hence so is the collision-induced angular momentum, $\boldsymbol{N'}$, as $\boldsymbol{L'}$ and $\boldsymbol{N'}$ must sum to give $\boldsymbol{J}$. $\boldsymbol{N'}$ perpendicular to **k** yields a limiting negative $A_0^{\{2\}}(\theta)$. However, despite this requirement, previous measurements of angle-resolved rotational alignments in NO(X) + Ar and Kr scattering have not always reached this limit.[7, 9, 16] A variety of possible causes have been suggested, included secondary collisions and depolarization via stray magnetic fields. We note that our experimental approach, with a well-defined and limited lifetime (≤ 400 ns) of the NO(A) before probing, appears to be unaffected by these issues.

Finally for NO(A) + He, we discuss briefly the $A_{1+}^{\{2\}}(\theta)$ results. These showed the worst agreement overall with the QS calculations. Although they are of the same sign, experiment generally reports a larger positive $A_{1+}^{\{2\}}(\theta)$ than that predicted, although for a few product states, e.g. N' = 9 and 10, the QS and experiment are the same within measurement errors. The $A_{1+}^{\{2\}}(\theta)$ moment is present in the data as a difference between the left and right halves of the scattering image about **k**, with a maximum sensitivity at the edges of the images, where the azimuthal scattering angle, φ, is 0° or 180°. This sensitivity for $A_{1+}^{\{2\}}(\theta)$ is the same for both of the H and V geometries. As the reported error bars suggest, with the 67° angle between **k**

and the probe laser propagation direction, $\mathbf{k_p}$, we have very similar sensitivities to the $A_{2+}^{\{2\}}(\theta)$ and $A_{1+}^{\{2\}}(\theta)$ moments in this experiment, and it is therefore perhaps surprising that we do not see a similar level of agreement with the QS calculations for both moments. Because the experimental images for different states were acquired in a pseudo-randomly interleaved fashion, so that images for states yielding better agreement for $A_{1+}^{\{2\}}(\theta)$ with QS calculations (e.g. $N' = 9$, 10) were acquired on the same day as those with poorer agreement (e.g. $N' = 6$, 8), we do not believe that this is the result of a systematic experimental artefact. Instead, we believe that this is a consequence of the lack of H/V geometry sensitivity in the $A_{1+}^{\{2\}}(\theta)$ measurement. Small changes in the experimental conditions during image acquisition, for example, a slow drift of the pump laser wavelength or energy, will tend to effect one side of the image more than the other. This is a consequence of the sequential wavelength scans of the probe laser necessary to avoid Doppler selection of the scattered NO. In our experimental geometry, and with wavelength scans in a consistent direction, the left-hand side of the images is on average acquired earlier in every acquisition cycle. Small imbalances between the left-hand and right-hand sides of the image have little effect on the extracted DCS, as it is determined by both sides equally. Similarly, $A_0^{\{2\}}(\theta)$ and $A_{2+}^{\{2\}}(\theta)$ have the same dependence on the two sides of the image, and are determined by the relative changes induced by the H/V polarization geometry. In contrast, $A_{1+}^{\{2\}}(\theta)$ depends purely on the difference between the two sides of the image, with the same sensitivity for the H and V geometries. Thus the determination of the $A_{1+}^{\{2\}}(\theta)$ moment is more sensitive to small fluctuations in the experimental conditions than that of the $A_0^{\{2\}}(\theta)$ and $A_{2+}^{\{2\}}(\theta)$ moments. As a result the quoted experimental error bars on $A_{1+}^{\{2\}}(\theta)$, which represent the statistical fluctuation in the 4 independent measurements, almost certainly understate the true measurement errors for this moment. As a result of this increased uncertainty in the measurement of $A_{1+}^{\{2\}}(\theta)$ in comparison to $A_0^{\{2\}}(\theta)$ and $A_{2+}^{\{2\}}(\theta)$, we do not reflect further on the significance of the $A_{1+}^{\{2\}}(\theta)$ results.

Turning to the experimental results for RET of NO(A) in collisions with D_2, we again note that there is no currently available PES for the NO(A)-H_2 system. We therefore confine the comparison of the experimental results for NO(A)-D_2 to those for the NO(A)-He system, from which we hope to gain some insight into the form of the NO(A)-D_2 PES. The qualitative behavior of the DCS for the two collision partners is broadly very similar, but for D_2 the maximum occurs at consistently more forward scattering angles for all final N'. This is very similar to the behavior observed by Gijsbertsen and coworkers for Λ-doublet state-selected NO(X) in collisions with He and D_2.[38] The structure in the DCSs is an example of a rotational rainbow, where collisions at different classical impact parameters lead to scattering at the same final angle. Gijsbertsen and coworkers used a simple 2-D classical model of the NO(X) + He scattering, and showed that an ellipsoidal,

hard shell, PES that agreed well with the equipotential at the mean collision energy on the *ab initio* NO(X)-He PES reproduced the observed rainbow angles.[38, 61] A similar calculation to fit the observed rainbow angles in NO(X) + D_2 required a larger difference between the major and minor axes of the ellipsoid, corresponding to a more anisotropic PES. Whilst the *ab initio* PES for NO(A)-He is clearly not well described by a rigid ellipsoid, the same basic principle should be in effect; and the rainbow maxima appearing at smaller, more forward, scattering angles indicate a more anisotropic PES for NO(A)-D_2 in comparison to NO(A)-He.[48] In the NO(A)-Ar system, we observed a very sharp peak in the extreme forward scattered region (e.g. in the 0-10° range), which was identifiable as the result of a relatively shallow (≈ -70 cm^{-1}) well in the NO(A)-Ar PES, localized at the N-end of the molecule.[43] The absence of any such forward peak at low-N' for NO(A) + D_2 scattering suggests that no such well is present in the NO(A)-D_2 PES, and that any attractive regions of the PES are largely isotropic with respect to the NO(A).

The rotational alignment parameters, $A_0^{\{2\}}(\theta)$ and $A_{2+}^{\{2\}}(\theta)$, determined for NO(A) + D_2 scattering are generally very similar to those observed for scattering from He. There is a systematic trend for $A_0^{\{2\}}(\theta)$ for scattering from D_2 to be less negative than that observed for scattering from He. In general, this results in the NO(A) + D_2 $A_0^{\{2\}}(\theta)$ being in better agreement with the predictions of the KA model. A naïve conclusion might be that the NO(A)-D_2 PES is more rigid than the NO(A)-He PES, leading to behavior more consistent with the KA model. However, it seems unlikely to us, *a priori*, that the more polarizable D_2 will result in a more rigid PES. Another possibility is that the more anisotropic NO(A)-D_2 PES results in RET from interactions over a smaller effective range of R, resulting in the KA-like behavior extending to higher product N'. A final possibility is simply that the anisotropic D_2 leads in general to a lower magnitude in alignment than the isotropic He from the collisions, which would also tend to draw the alignment moments, essentially fortuitously, into closer agreement with the KA model.

The comparison of the NO(A) + D_2 and NO(A) + He scattering dynamics has enabled us to draw some conclusions about the form of the NO(A)-D_2 PES as a function of NO(A) orientation with respect to D_2, but up to this point we have implicitly assumed that the D_2 is itself isotropic, like the He. Anisotropy in the PES dependent on the orientation of the D_2 with respect to the NO(A) would be expected to result in rotational excitation of the D_2 in the collision, which would be revealed in the experiments as a decrease in the kinetic energy release to NO(A). We see no evidence for rotational excitation of the D_2 in any of the NO(A) product N' states. We have chosen to illustrate this with N' = 12 because we believe that the low impact parameter, backward-scattered, collisions yielding the highest-N' product NO states are the most likely to simultaneously rotationally excite the D_2. Assuming a collision energy of 670 cm^{-1}, the available energy to go into translation or D_2 rotation

is 358 cm^{-1}, sufficient, as we show below, for excitation of several D_2 rotational levels. Fig. 6 (a) shows the total sum of all of the V and H geometry images recorded for scattering from D_2 to $N' = 12$, on which is superimposed a Newton diagram and scattering rings showing the in-plane scattering velocities consistent with the various possible RET process among the $j = 0$ - 3 rotational states of D_2. The nuclear spin of D, $I = 1$, results in ortho and para states of D_2, and because the nuclear spin is only very weakly coupled to the nuclear rotation, we expect to only observe even changes in the D_2 rotational quantum number, j. Since the D_2 rotational constant is large, $B = 30.443$ cm^{-1}, RET of D_2 involves significant energy gaps relative to the experimental collision energy, and thus with 312 cm^{-1} already partitioned into NO rotation for $N' = 12$, only a few D_2 transitions are possible.[62] With measureable initial D_2 population only being present in $j = 0$, 1 and 2, in an estimated ratio of 0.68:0.26:0.06,[49] we expect to only be able to observe $\Delta j \neq 0$ transitions from $j = 0 \rightarrow 2$, $j = 1 \rightarrow 3$, and $j = 2 \rightarrow 0$. However, Fig. 6(a) provides no clear evidence for scattering signal with kinetic energies consistent with D_2 RET. Fig. 6(b) shows the residual from a fit to the averaged data, assuming that no D_2 RET occurs. We would expect that any D_2 RET occurring would be manifest in a systematic non-zero residual between the fitted image and the experimental data. By comparing the sum of the residuals to the total experimental image intensity we estimate the contribution to the scattering image from D_2 RET to be ≤ 3 % for the NO(A) $N' = 12$ state. No evidence for D_2 RET is provided by inspection of the residuals from similar fits to the averaged data for any of the other product N', leading us to conclude that there is no significant rotational excitation of D_2 in collisions with NO(A) at this collision energy. This implies that the NO(A)-D_2 PES displays low anisotropy with respect to D_2 orientation relative to NO(A), resulting in no mechanism for rotational excitation of the D_2.

V. CONCLUSIONS

We have reported state-to-state DCSs and angle-resolved rotational angular momentum polarization moments for RET in collisions of NO(A) with He and D_2 with near-identical collision energy distributions. The DCSs for both systems display single rotational rainbow maxima that peak at progressively larger scattering angles with increasing N'. The angular momentum polarization moments show behavior which departs significantly from the predictions of the kinematic apse model of the collisions, with the disagreement increasing at higher N'. QS calculations using a recent NO(A)-He PES show excellent agreement with the measured DCS, and agree well with the rotational angular momentum polarization moments. This confirms that the PES calculated by Kłos *et al* provides an excellent representation of the NO(A)-He interaction within the collision energy range probed in these experiments. Comparison of the observed scattering dynamics with D_2 and He provides information on the hitherto unknown NO(A)-D_2 PES. The qualitatively similar forms of the DCSs and broad similarities between the rotational polarization moments for the two colliders suggest that the PESs are in general also

similar. The rainbow maxima for scattering from D_2 appear at smaller, more forward, angles than those from He, consistent with the NO(A)-D_2 PES being more anisotropic than the NO(A)-He PES. No evidence for significant RET in the D_2 collision partner is observed within experimental uncertainty. We hope that these detailed first measurements of the dynamics of NO(A)+D_2 RET provide a stimulus for the extension of electronic structure calculations from NO(A) + Rg systems to simple NO(A) + diatomic systems.

ACKNOWLEDGEMENTS

This work was supported by the U.K. EPSRC *via* grant EP/J017973/01 to M.L.C, K.G.M. and D.T. T.F.M.L. acknowledges Heriot-Watt University for a James Watt PhD scholarship. We also acknowledge the assistance of P. J. Dagdigian, J. Kłos and M. H. Alexander in performing the quantum scattering calculations. Raw data on which this publication is based can be accessed via the Heriot-Watt University Data Repository.

REFERENCES

1. A. Schiffman and D. W. Chandler, Int Rev Phys Chem **14**, 371 (1995).
2. P. J. Dagdigian, in *The Chemical Dynamics and Kinetics of Small Radicals*, Advanced Series in Physical Chemistry, edited by K. Liu and A. J. Wagner (World Scientific, Singapore, 1995), p. 315.
3. G. Paterson, M. L. Costen, and K. G. McKendrick, Int Rev Phys Chem **31**, 69 (2012).
4. H. Chadwick, M. Brouard, T. Perkins, and F. J. Aoiz, Int Rev Phys Chem **33**, 79 (2014).
5. M. L. Costen, S. Marinakis, and K. G. McKendrick, Chem Soc Rev **37**, 732 (2008).
6. M. N. R. Ashfold, N. H. Nahler, A. J. Orr-Ewing, O. P. J. Vieuxmaire, R. L. Toomes, T. N. Kitsopoulos, I. A. Garcia, D. A. Chestakov, S. M. Wu, and D. H. Parker, Phys Chem Chem Phys **8**, 26 (2006).
7. E. A. Wade, K. T. Lorenz, D. W. Chandler, J. W. Barr, G. L. Barnes, and J. I. Cline, Chem Phys **301**, 261 (2004).
8. K. T. Lorenz, D. W. Chandler, J. W. Barr, W. W. Chen, G. L. Barnes, and J. I. Cline, Science **293**, 2063 (2001).
9. M. Brouard, H. Chadwick, C. J. Eyles, B. Hornung, B. Nichols, F. J. Aoiz, P. G. Jambrina, and S. Stolte, J Chem Phys **138**, 104310 (2013).
10. A. G. Suits, L. S. Bontuyan, P. L. Houston, and B. J. Whitaker, J Chem Phys **96**, 8618 (1992).
11. L. S. Bontuyan, A. G. Suits, P. L. Houston, and B. J. Whitaker, J Phys Chem **97**, 6342 (1993).
12. A. A. Dixit, P. J. Pisano, and P. L. Houston, J Phys Chem A **105**, 11165 (2001).
13. H. Kohguchi, T. Suzuki, and M. H. Alexander, Science **294**, 832 (2001).
14. B. Nichols, H. Chadwick, S. D. S. Gordon, C. J. Eyles, B. Hornung, M. Brouard, M. H. Alexander, F. J. Aoiz, A. Gijsbertsen, and S. Stolte, Chem Sci **6**, 2202 (2015).
15. H. Chadwick, B. Nichols, S. D. S. Gordon, B. Hornung, E. Squires, M. Brouard, J. Kłos, M. H. Alexander, F. J. Aoiz, and S. Stolte, J Phys Chem Lett **5**, 3296 (2014).
16. M. Brouard, H. Chadwick, S. D. S. Gordon, B. Hornung, B. Nichols, J. Kłos, F. J. Aoiz, and S. Stolte, J Chem Phys **141**, 164306 (2014).
17. M. Brouard, H. Chadwick, C. J. Eyles, B. Hornung, B. Nichols, J. M. Scott, F. J. Aoiz, J. Kłos, S. Stolte, and X. Zhang, Mol Phys **111**, 1759 (2013).
18. C. J. Eyles, M. Brouard, H. Chadwick, B. Hornung, B. Nichols, C. H. Yang, J. Kłos, F. J. Aoiz, A. Gijsbertsen, A. E. Wiskerke, and S. Stolte, Phys Chem Chem Phys **14**, 5403 (2012).
19. C. J. Eyles, M. Brouard, H. Chadwick, F. J. Aoiz, J. Kłos, A. Gijsbertsen, X. Zhang, and S. Stolte, Phys Chem Chem Phys **14**, 5420 (2012).
20. C. J. Eyles, M. Brouard, C. H. Yang, J. Kłos, F. J. Aoiz, A. Gijsbertsen, A. E. Wiskerke, and S. Stolte, Nat Chem **3**, 597 (2011).

21. F. J. Aoiz, J. E. Verdasco, M. Brouard, J. Klos, S. Marinakis, and S. Stolte, J Phys Chem A **113**, 14636 (2009).
22. J. Kłos, F. J. Aoiz, J. E. Verdasco, M. Brouard, S. Marinakis, and S. Stolte, J Chem Phys **127**, 031102 (2007).
23. G. Sarma, S. Marinakis, J. J. ter Meulen, D. H. Parker, and K. G. McKendrick, Nat Chem **4**, 985 (2012).
24. A. G. Suits, C. K. Bishwakarma, L. Song, G. C. Groenenboom, A. van der Avoird, and D. H. Parker, J Phys Chem A **119**, 5925 (2015).
25. K. T. Lorenz, D. W. Chandler, and G. C. McBane, J Phys Chem A **106**, 1144 (2002).
26. J. Onvlee, S. N. Vogels, A. D. van der Avoird, G. C. Groenenboom, and S. Y. T. van de Meerakker, New J Phys **17**, 055019 (2015).
27. A. von Zastrow, J. Onvlee, S. N. Vogels, G. C. Groenenboom, A. van der Avoird, and S. Y. T. van de Meerakker, Nat Chem **6**, 216 (2014).
28. S. N. Vogels, J. Onvlee, S. Chefdeville, A. van der Avoird, G. C. Groenenboom, and S. Y. T. van de Meerakker, Science **350**, 787 (2015).
29. U. Buck, F. Huisken, J. Schleusener, and J. Schaefer, J Chem Phys **74**, 535 (1981).
30. U. Buck, F. Huisken, and J. Schleusener, J Chem Phys **68**, 5654 (1978).
31. J. A. Bacon, C. F. Giese, and W. R. Gentry, J Chem Phys **108**, 3127 (1998).
32. M. T. Vonk, J. A. Bacon, C. F. Giese, and W. R. Gentry, J Chem Phys **106**, 1353 (1997).
33. O. Tkac, Q. L. Ma, M. Stei, A. J. Orr-Ewing, and P. J. Dagdigian, J Chem Phys **142**, 10 (2015).
34. O. Tkac, A. K. Saha, J. Loreau, Q. L. Ma, P. J. Dagdigian, D. H. Parker, A. van der Avoird, and A. J. Orr-Ewing, Mol Phys **113**, 3925 (2015).
35. O. Tkac, A. J. Orr-Ewing, P. J. Dagdigian, M. H. Alexander, J. Onvlee, and A. van der Avoird, J Chem Phys **140**, 134308 (2014).
36. O. Tkac, Q. L. Ma, C. A. Rusher, S. J. Greaves, A. J. Orr-Ewing, and P. J. Dagdigian, J Chem Phys **140**, 204318 (2014).
37. O. Tkac, A. G. Sage, S. J. Greaves, A. J. Orr-Ewing, P. J. Dagdigian, Q. L. Ma, and M. H. Alexander, Chem Sci **4**, 4199 (2013).
38. A. Gijsbertsen, H. Linnartz, and S. Stolte, J Chem Phys **125**, 133112 (2006).
39. M. S. Westley, K. T. Lorenz, D. W. Chandler, and P. L. Houston, J Chem Phys **114**, 2669 (2001).
40. J. D. Steill, J. J. Kay, G. Paterson, T. R. Sharples, J. Kłos, M. L. Costen, K. E. Strecker, K. G. McKendrick, M. H. Alexander, and D. W. Chandler, J Chem Phys A **117**, 8163 (2013).
41. J. J. Kay, J. D. Steill, J. Kłos, G. Paterson, M. L. Costen, K. E. Strecker, K. G. McKendrick, M. H. Alexander, and D. W. Chandler, Mol Phys **110**, 1693 (2012).
42. J. J. Kay, G. Paterson, M. L. Costen, K. E. Strecker, K. G. McKendrick, and D. W. Chandler, J Chem Phys **134**, 091101 (2011).
43. T. R. Sharples, T. F. M. Luxford, D. Townsend, K. G. McKendrick, and M. L. Costen, J Chem Phys **143**, 204301 (2015).
44. W. G. Bessler, C. Schulz, T. Lee, J. B. Jeffries, and R. K. Hanson, Appl Optics **42**, 4922 (2003).
45. A. F. H. van Gessel, K. M. J. Alards, and P. J. Bruggeman, J Phys D Appl Phys **46**, 265202 (2013).
46. R. P. Wayne, *Chemistry of Atmospheres,* Third ed. (Oxford University Press, Oxford, 2000).
47. J. A. Miller and C. T. Bowman, Prog Energ Combust **15**, 287 (1989).
48. J. Kłos, M. H. Alexander, R. Hernandez-Lamoneda, and T. G. Wright, J Chem Phys **129**, 244303 (2008).
49. See the Supplemental Material at DOI xxxx for additional information.
50. HIBRIDON is a package of programs for the time-independent quantum treatment of inelastic collisions and photodissociation written by M. H. Alexander, D. E. Manolopoulos, H.-J. Werner, B. Follmeg, and P. J. Dagdigian, with contributions by D. Lemoine, P. Vohralik, G. Corey, B. Johnson, T. Orlikowski, A. Berning, A. Degli-Esposti, C. Rist, B. Pouilly, J. Kłos, Q. Ma, G. van der Sanden, M. Yang, F. de Weerd, S. Gregurick, and F. Lique. More information and/or a copy of the code can be obtained from the website http://www2.chem.umd.edu/groups/alexander/hibridon/hib43.
51. I. V. Hertel and W. Stoll, in *Adv At Mol Phys*, edited by D. R. Bates and B. Benjamin (Academic Press, 1978) Volume 13, p. 113.
52. R. C. Woods and T. A. Dixon, J Chem Phys **64**, 5319 (1976).
53. V. Khare, D. J. Kouri, and D. K. Hoffman, J Chem Phys **74**, 2275 (1981).
54. U. Fano and J. H. Macek, Rev Mod Phys **45**, 553 (1973).
55. K. L. Reid, Chem Phys Lett **215**, 25 (1993).
56. R. Altkorn, R. N. Zare, and C. H. Greene, Mol Phys **55**, 1 (1985).
57. J. A. Guest, M. A. Ohalloran, and R. N. Zare, Chem Phys Lett **103**, 261 (1984).
58. W. H. Press, S. A. Teukolsky, W. T. Vetterling, and B. P. Flannery, *Numerical Recipes in Fortran 90* (Cambridge University Press, Cambridge, 1996).
59. M. Brouard, H. Chadwick, C. J. Eyles, B. Hornung, B. Nichols, F. J. Aoiz, P. G. Jambrina, S. Stolte, and M. P. de Miranda, J Chem Phys **138**, 104309 (2013).
60. J. Klos, G. Chalasinski, M. T. Berry, R. Bukowski, and S. M. Cybulski, J Chem Phys **112**, 2195 (2000).
61. S. Bosanac, Phys Rev A **22**, 2617 (1980).

62. K. P. Huber and G. Herzberg, *Molecular Spectra and Molecular Structure IV. Constants of Diatomic Molecules* (Van Nostrand Reinhold, Princeton, 1979).

TABLE I. Definitions and classical limiting values of Hertel – Stoll normalized polarization parameters, $A_{q+}^{\{2\}}$.

Moment	Definition	Classical Limits[a]
$A_0^{\{2\}}$	$\dfrac{\left\langle 3j_z - \mathbf{j}^2 \right\rangle}{\left\langle jm\left\vert \mathbf{j}^2 \right\vert jm \right\rangle}$	$+2$, $\mathbf{j} \parallel \mathbf{z}$ -1, $\mathbf{j} \perp \mathbf{z}$
$A_{1+}^{\{2\}}$	$\dfrac{\sqrt{3}\left\langle j_x j_z + j_z j_x \right\rangle}{\left\langle jm\left\vert \mathbf{j}^2 \right\vert jm \right\rangle}$	$+\sqrt{3}$, $\mathbf{j} \parallel (\mathbf{x} + \mathbf{z})$ $-\sqrt{3}$, $\mathbf{j} \parallel (\mathbf{x} - \mathbf{z})$
$A_{2+}^{\{2\}}$	$\dfrac{\sqrt{3}\left\langle j_x{}^2 - j_y{}^2 \right\rangle}{\left\langle jm\left\vert \mathbf{j}^2 \right\vert jm \right\rangle}$	$+\sqrt{3}$, $\mathbf{j} \parallel \mathbf{x}$ $-\sqrt{3}$, $\mathbf{j} \parallel \mathbf{y}$

[a] $\parallel$ and $\perp$ refer to distributions of **j** that are aligned maximally parallel and perpendicular to the given axes. **x**, **y** and **z** are unit vectors along the x, y and z axes, respectively.

Figure Captions

Figure 1. Newton diagrams for collisions of NO(A) with (a) He and (b) D_2 as performed in this study, overlaid on V+H geometry summed images of product state $N' = 8$. Arrows indicate the initial velocity vectors of the colliders; $\mathbf{v_{NO}}$, $\mathbf{v_{He}}$ or $\mathbf{v_{D2}}$, the center of mass velocity $\mathbf{v_{cm}}$ and the relative velocity $\mathbf{k}$. The average final velocity of NO scattered in the plane of the detector is indicated by the ring. The offset arrow towards the bottom of each panel shows the propagation direction of the probe laser beam, $\mathbf{k_p}$.
(Single column)

Figure 2. Example single measurement experimental images for rotational energy transfer of NO(A, v = 0, $N = 0, j = 0.5$) to final states NO(A, v = 0, $N' = 3$, 5-12) in collisions with He at an average collision energy of 670 cm^{-1}, together with the images resulting from the fitting procedure. 1st column, experimental V-geometry; 2nd column fit V-geometry; 3rd column experimental H-geometry; 4th column fit H-geometry.

(Single column)

Figure 3. Example single measurement experimental images for rotational energy transfer of NO(A, v = 0, $N = 0, j = 0.5$) to final states NO(A, v = 0, $N' = 3$, 5-12) in collisions with D_2 at an average collision energy of 663 cm^{-1}, together with the images resulting from the fitting procedure. 1st column, experimental V-geometry; 2nd column fit V-geometry; 3rd column experimental H-geometry; 4th column fit H-geometry.
(Single column)

Figure 4: Differential cross sections and angular momentum alignment moments, $A_{q+}^{\{2\}}(\theta)$, for rotational energy transfer of NO(A, v = 0, $N = 0, j = 0.5$) to final states NO(A, v = 0, $N' = 3$, 5-12) in collisions with He. 1st column, differential cross sections; 2nd column $A_0^{\{2\}}(\theta)$; 3rd column $A_{1+}^{\{2\}}(\theta)$; 4th column $A_{2+}^{\{2\}}(\theta)$. Results of fitting to the experimental images (solid black line, error bars represent 95% confidence limits), collision-energy averaged quantum scattering calculations (dashed blue line), and for $A_{q+}^{\{2\}}(\theta)$ moments, collision-energy averaged kinematic apse model calculations (dotted green line).
(Double column)

Figure 5: Differential cross sections and angular momentum alignment moments, $A_{q+}^{\{2\}}(\theta)$, for rotational energy transfer of NO(A, v = 0, $N = 0, j = 0.5$) to final states NO(A, v = 0, $N' = 3$, 5-12) in collisions with D_2. 1st column, differential cross sections; 2nd column $A_0^{\{2\}}(\theta)$; 3rd column $A_{1+}^{\{2\}}(\theta)$; 4th column $A_{2+}^{\{2\}}(\theta)$. Results of fitting to the experimental images (solid red line, error bars represent 95% confidence limits), fit results for collisions with He (also shown in Fig. 4, solid black line), and for $A_{q+}^{\{2\}}(\theta)$ moments, collision-energy averaged kinematic apse model calculations (dotted green line).
(Double column)

Figure 6. (a) Experimental V+H geometry summed image from rotational energy transfer from Newton diagram for rotational energy transfer of NO(A, v = 0, $N = 0, j = 0.5$) to final state NO(A, v = 0, $N' = 12$) in collisions with D_2. Overlaid white lines indicate the average Newton diagram collision vectors, together with scattering rings showing the final in-plane NO velocity corresponding to coincident rotational energy transfer in D_2 ($j \rightarrow j'$). From largest to smallest rings: $2 \rightarrow 0$, $0 \rightarrow 0$, $0 \rightarrow 2$, and $1 \rightarrow 3$. (b) Residual V+H geometry summed image resulting from subtraction of best fit simulated image from the experimental data image shown in (a), overlaid with the same Newton diagram vectors and scattering rings.
(Single column)

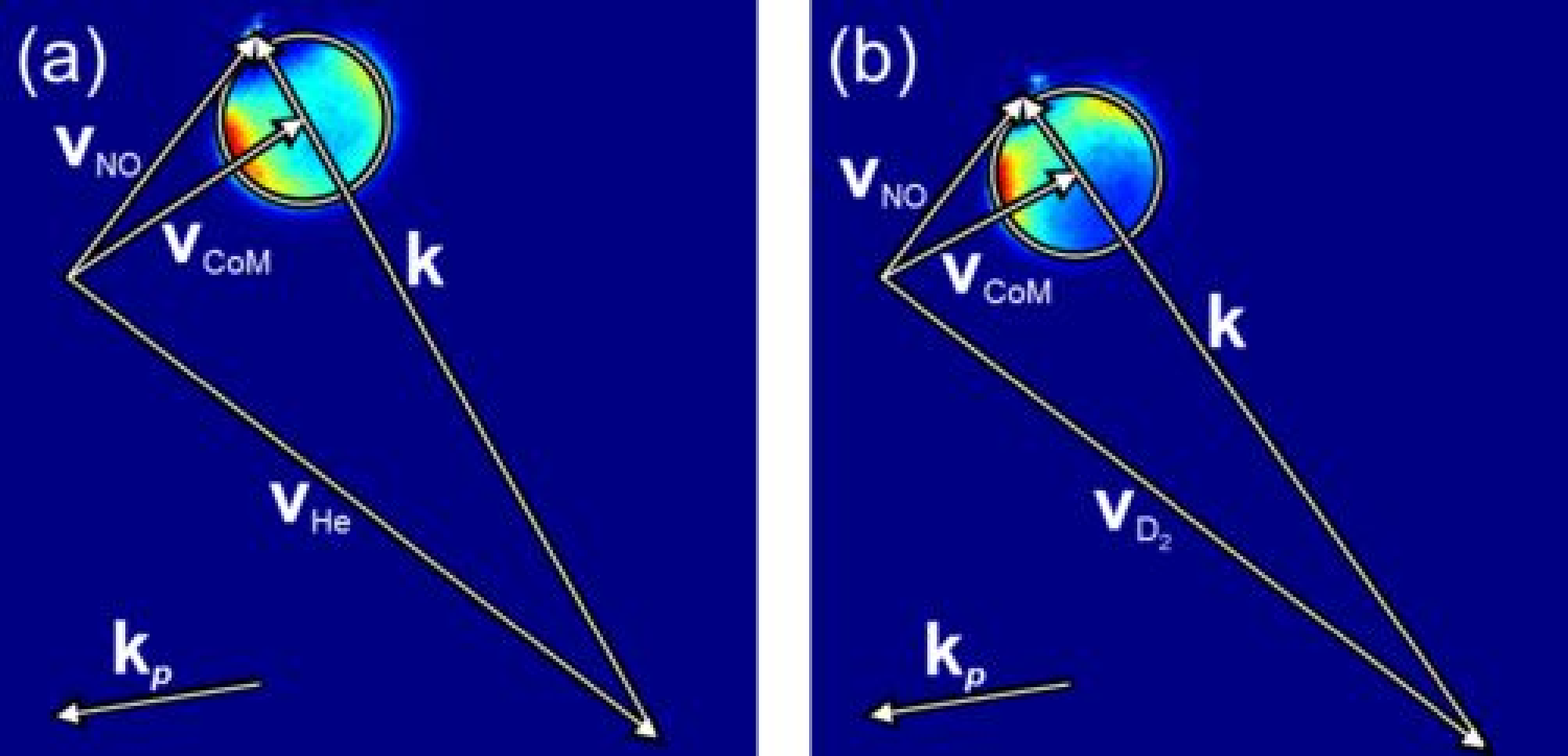
(a)
$\mathbf{v}_{NO}$
$\mathbf{v}_{CoM}$
$\mathbf{k}$
$\mathbf{v}_{He}$
$\mathbf{k}_p$
(b)
$\mathbf{v}_{NO}$
$\mathbf{v}_{CoM}$
$\mathbf{k}$
$\mathbf{v}_{D_2}$
$\mathbf{k}_p$

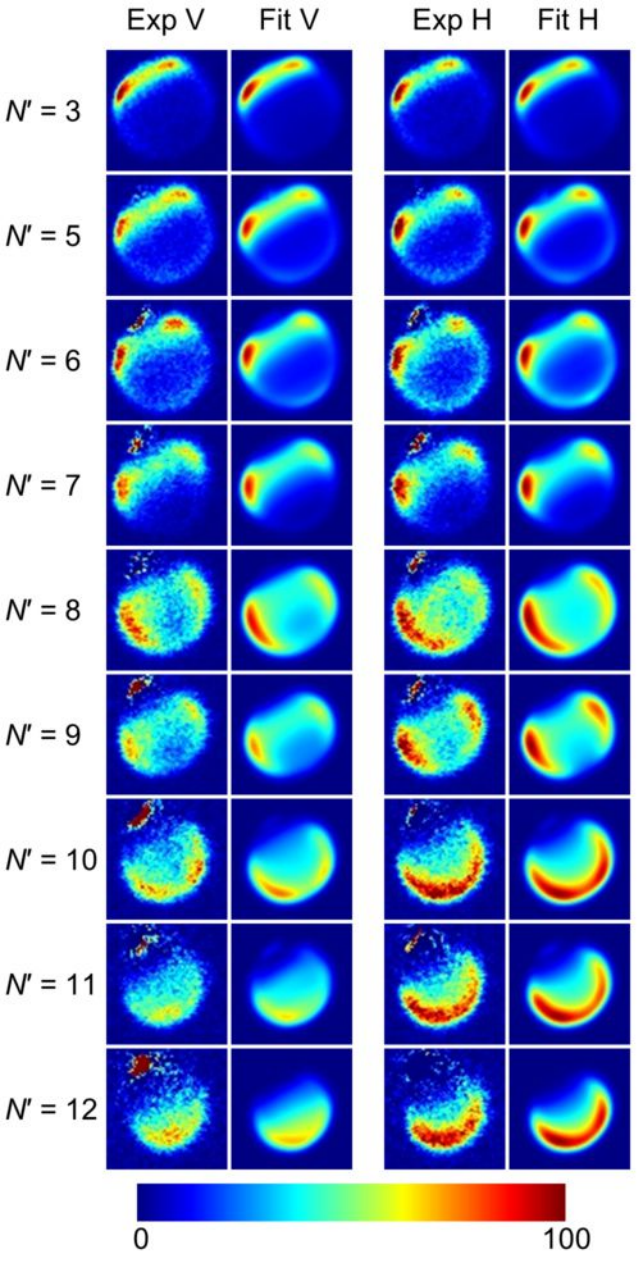
Exp V
Fit V
Exp H
Fit H
N′ = 3
N′ = 5
N′ = 6
N′ = 7
N′ = 8
N′ = 9
N′ = 10
N′ = 11
N′ = 12
0
100

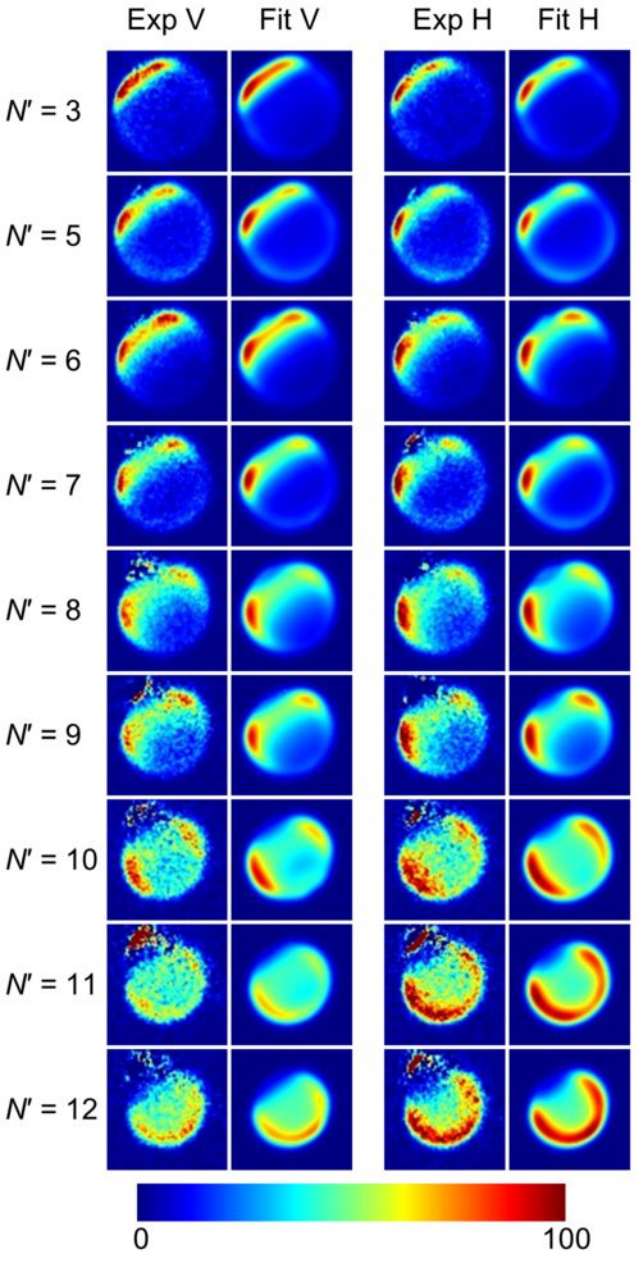
Exp V
Fit V
Exp H
Fit H
N′ = 3
N′ = 5
N′ = 6
N′ = 7
N′ = 8
N′ = 9
N′ = 10
N′ = 11
N′ = 12
0
100

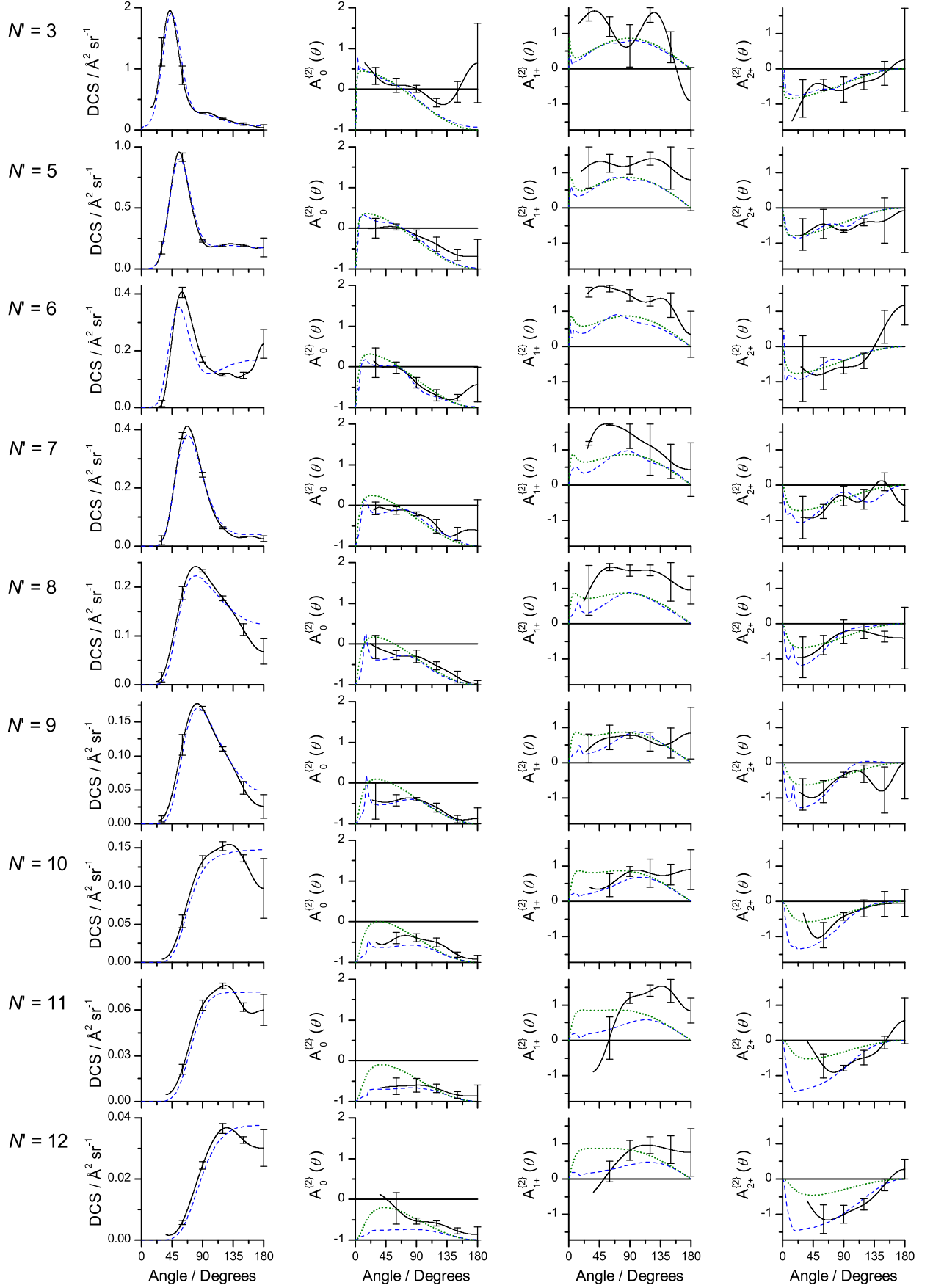
N' = 3
N' = 5
N' = 6
N' = 7
N' = 8
N' = 9
N' = 10
N' = 11
N' = 12
DCS / Å² sr⁻¹
A₀^(2) (θ)
A₁₊^(2) (θ)
A₂₊^(2) (θ)
0 45 90 135 180
Angle / Degrees

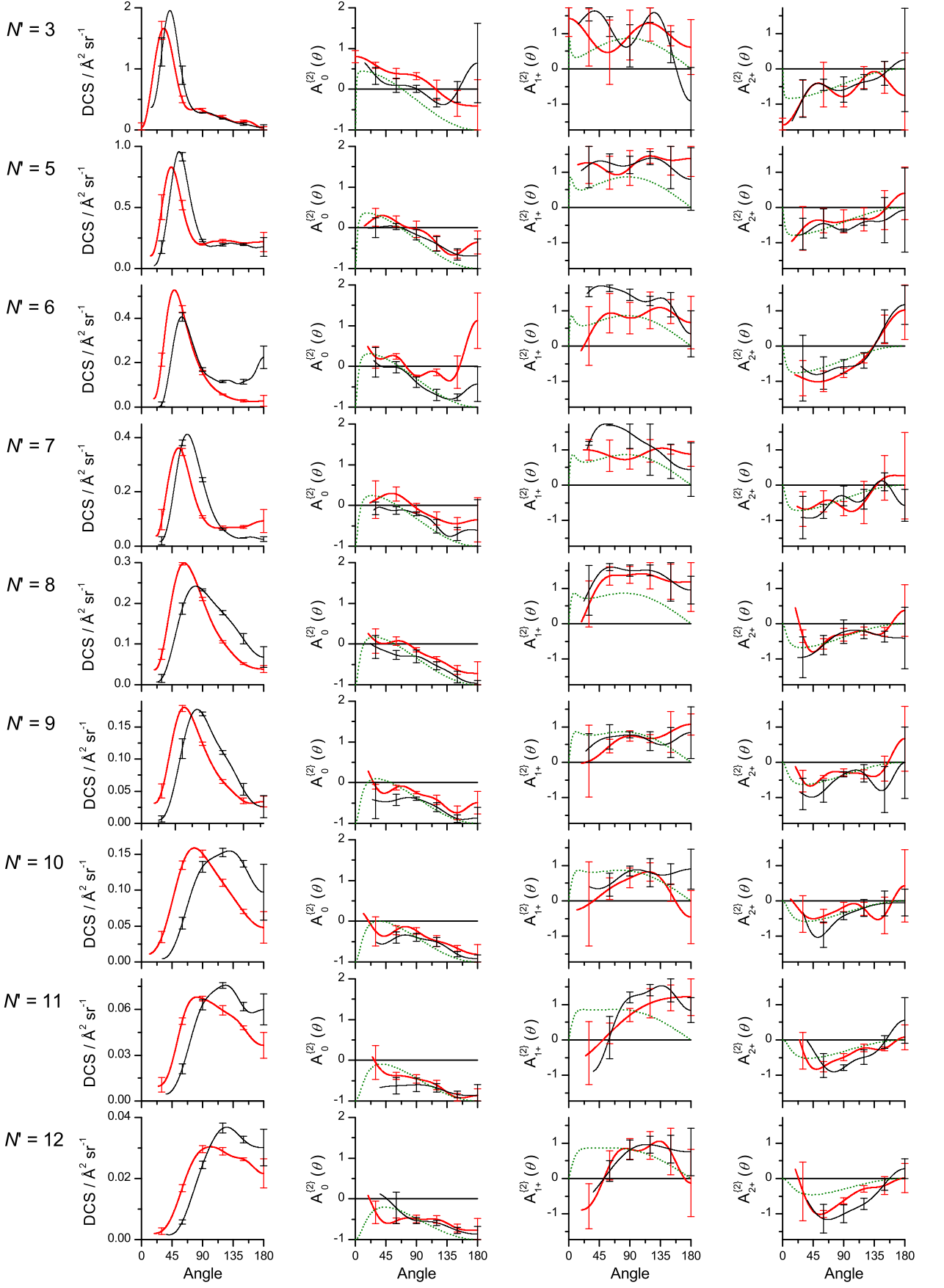
N' = 3
N' = 5
N' = 6
N' = 7
N' = 8
N' = 9
N' = 10
N' = 11
N' = 12
DCS / Å^2 sr^{-1}
$A_0^{(2)}(\theta)$
$A_{1+}^{(2)}(\theta)$
$A_{2+}^{(2)}(\theta)$
Angle
0
45
90
135
180

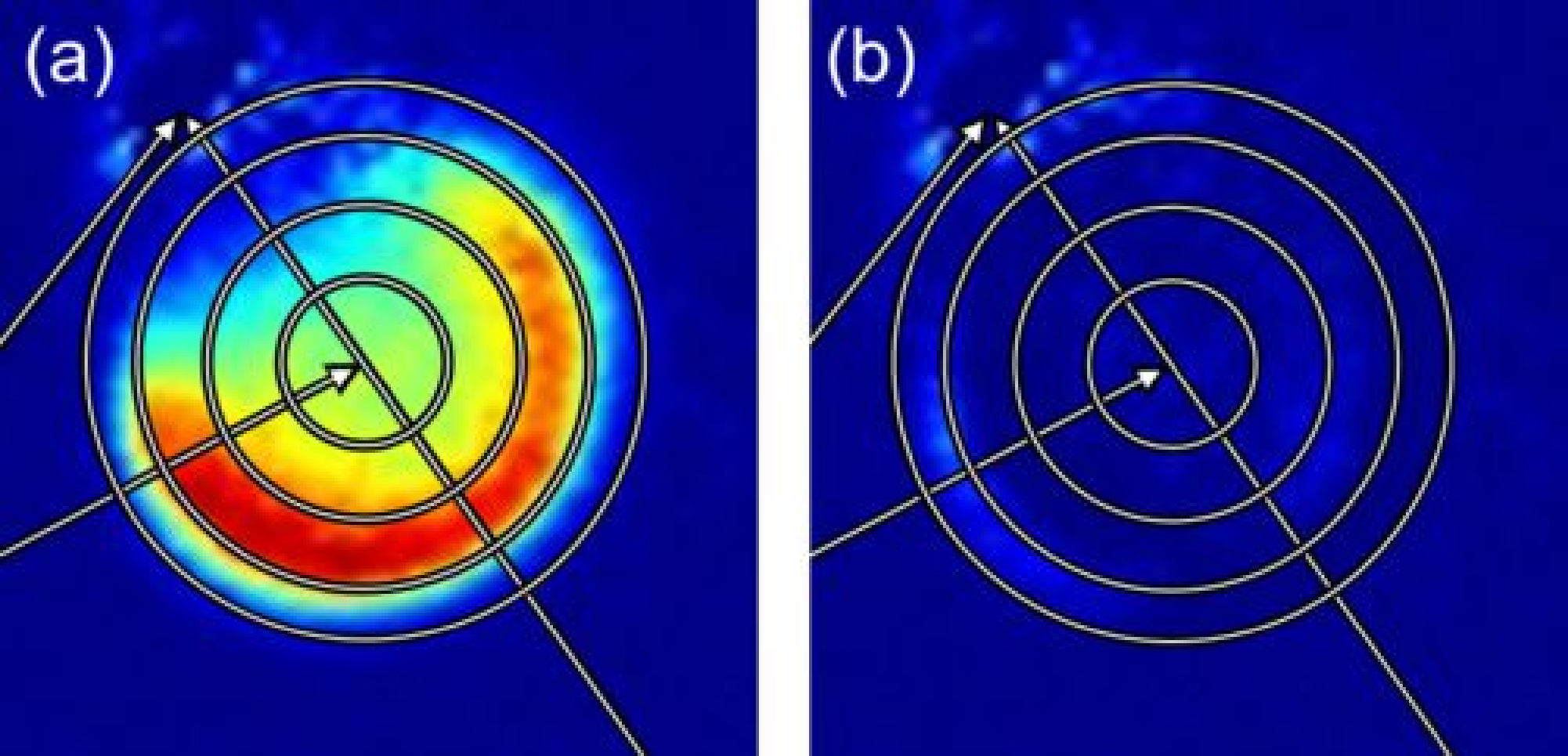
(a)
(b)